

Obscuration in high redshift jetted QSO

A. Caccianiga^{*1}, L. Ighina^{1,2,3}, A. Moretti¹, R. Brivio^{1,2}, S. Belladitta^{4,5}, D. Dallacasa^{6,7}, C. Spingola⁷, M.J. Marchã⁸, and S. Antón⁹

¹ INAF - Osservatorio Astronomico di Brera, via Brera 28, I-20121 Milan, Italy

² DiSAT, Università degli Studi dell'Insubria, via Valleggio 11, 22100 Como, Italy

³ International Centre for Radio Astronomy Research, Curtin University, 1 Turner Avenue, Bentley, WA, 6102, Australia

⁴ Max Planck Institut für Astronomie, Königstuhl 17, 69117 Heidelberg, Germany

⁵ INAF – Osservatorio di Astrofisica e Scienza dello Spazio, Via Gobetti 93/3, 40129 Bologna, Italy

⁶ Dipartimento di Astronomia, Università di Bologna, via Ranzani 1, 40127, Bologna, Italy

⁷ INAF - Istituto di Radioastronomia, Via Gobetti 101, I-40129 Bologna, Italy

⁸ Dept. of Physics&Astronomy and Dept. of Computer Science, University College London, Gower Street, London, WC1E 6BT, UK

⁹ Centro de Física da UC, Departamento de Física, Universidade de Coimbra, 3004-516 Coimbra, Portugal

Received XX; accepted yy

ABSTRACT

Context. Obscuration in high-redshift quasi-stellar objects (QSO) has a profound impact on our understanding of the evolution of supermassive black holes across the cosmic time. An accurate quantification of its relevance is therefore mandatory.

Aims. We present a study aimed at evaluating the importance of obscuration in high redshift jetted QSO, i.e. those active nuclei characterized by the presence of powerful relativistic jets.

Methods. We compare the observed number of radio detected QSO at different radio flux density limits with the value predicted by the beaming model on the basis of the number of oriented sources (blazars). Any significant deficit of radio-detected QSO compared to the predictions can be caused by the presence of obscuration along large angles from the jet direction. We apply this method to two sizable samples characterized by the same optical limit (mag=21) but significantly different radio density limits (30 mJy and 1 mJy respectively) and containing a total of 87 independent radio-loud $4 \leq z \leq 6.8$ QSO, 31 of which classified as blazars.

Results. We find a general good agreement between the numbers predicted by the model and those actually observed with only a marginal discrepancy at ~ 0.5 mJy that could be caused by the lack of completeness of the sample. We conclude that we have no evidence of obscuration within angles $10\text{--}20^\circ$ from the relativistic jet direction. We also show how the on-going deep wide-angle radio surveys will be instrumental to test the presence of obscuration at much larger angles, up to $30\text{--}35^\circ$. We finally suggest that, depending on the actual fraction of obscured QSO, relativistic jets could be much more common at high redshifts compared to what is usually observed in the local Universe.

Key words. galaxies: active – galaxies: high-redshift – galaxies: jets

1. Introduction

The study of the very first phase of the supermassive black hole (SMBH) growth represents a critical step for understanding the galaxy early evolution (e.g. Heckman & Best 2014; Merloni 2016). To this end, a reliable and complete census of the accreting SMBH, i.e. Active Galactic Nuclei (AGN), at high redshifts is mandatory (e.g. Bañados et al. 2016; Pacucci & Loeb 2021; Fan et al. 2022; Banados et al. 2022). For observational reasons, the study of high redshift accreting SMBHs is mostly limited to the part of the population residing in unabsorbed objects, the so-called type1 AGN, while SMBH embedded in absorbed systems (type 2 AGN) typically elude observations. Up to now, these elusive objects were nearly beyond the capabilities of the existing telescopes except for few possible examples (e.g. Endsley et al. 2022; Drouart et al. 2020), although their detection is now becoming possible thanks to the James Webb Space Telescope (e.g. Yang et al. 2023). For these reasons, most of the studies of the SMBH formation and evolution are still based on high redshift unobscured AGN and, therefore, they are potentially biased. Assuming for the high-z AGN the same obscured

fraction measured locally is too simplistic, since there are several pieces of evidence showing that the fraction of obscured sources significantly increases at high-z (see e.g. Zeimann et al. 2011; Moretti et al. 2012; Merloni et al. 2014; Aird et al. 2015; Gilli et al. 2022; Vijarnwannaluk et al. 2022; Yang et al. 2023).

The presence of a relativistic jet in AGN greatly helps to quantify the importance of obscuration. When an AGN of this type is observed close to the jet direction, its emission is significantly boosted due to relativistic beaming and the oriented nature of the source can be easily recognized. Such oriented sources are called blazars (see Urry & Padovani 1995 for a review). Notably, the particular orientation of blazars makes obscuration marginal, since the jet is expected to clear out the path along the line-of-sight. From a statistically complete sample of blazars, selected at a given radio limit, it is then possible to study the impact of the circum-nuclear obscuring medium since the detection of a blazar with a given radio flux density implies the existence of a well-defined number of misaligned sources at lower flux densities ($\sim 2\Gamma^2$, where Γ is the bulk Lorentz factor of the jet): A significant deficit of the observed misaligned sources, compared to the predictions, then implies the existence, at a certain critical angle, of an obscuration structure. Using this approach,

* alessandro.caccianiga@inaf.it

Ghisellini & Sbarato (2016) have pointed out the possible presence of an almost 4π obscuring structure around the most luminous jetted AGN, although this result was quite uncertain being based on a small sample of blazars.

It is important to note that, from the optical point of view, the class of blazars includes two different types of sources: 1) BL Lac objects, that are characterized by featureless optical spectra, and 2) flat-spectrum radio quasars (FSRQ), whose optical properties are similar to those observed in radio-quiet quasi-stellar objects (QSO), being usually dominated, at these wavelengths, by the accretion disk emission. The two types of blazars are likely associated to two different classes of jetted AGN, characterized by different physical properties, probably connected to the accretion rate on the central SMBH (e.g. Tadhunter 2016). Here, we only consider the class of FSRQ since BL Lac objects are usually not found at high redshifts (≥ 4) although the possible discovery of a BL Lac at $z \sim 6.57$ was recently claimed (Koptelova & Hwang 2022). Throughout the paper, we will use the term “QSO” to indicate an AGN with strong emission lines ($EW > 5\text{\AA}$) and/or a clear evidence of the accretion disk emission in the optical spectrum, regardless of its luminosity and/or the presence of a jet.

In this work, we use two sizable flux-limited samples of high redshift blazars to investigate the issue of obscuration in jetted QSO in the early Universe by adopting a statistical approach similar to that described in Ghisellini & Sbarato (2016). The first one is the CLASS (Cosmic Lens All Sky Survey) high- z QSO sample (Caccianiga et al. 2019; Ighina et al. 2019) which is characterized by a relatively high radio flux density limit (30 mJy) and an optical limit of $\text{mag}=21$, while the second one, based on data from the Faint Images of the Radio Sky at Twenty-Centimeters (FIRST) survey, has a much fainter radio flux density limit (0.5 mJy) but the same optical limit of CLASS. The combination of these two samples greatly increases the sensitivity to absorption effects and, at the same time, improves the statistics, making our study more accurate.

In Section 2 we discuss the method used to derive the expected number of jetted QSO from the observed number of oriented sources (blazars) in a flux-limited sample. We then apply this method to the CLASS sample (Section 3) and to the FIRST sample (Section 4). In Section 5 we discuss the expected improvements offered by incoming new surveys based on SKA precursors/pathfinders. Finally, in Section 6 we summarize our conclusions.

In the paper we use the mag_{drop} defined as the magnitude, in AB system and corrected for Galactic extinction, in the reddest filter of the dropout used to select the sources. This means the r -filter for $4 \leq z < 4.5$, the i -filter for $4.5 \leq z < 5.4$, the z -filter for $5.4 \leq z < 6.3$ and the y -filter for $z \geq 6.3$ objects. By construction, mag_{drop} corresponds to a quite narrow range of rest-frame wavelengths, between $\sim 1250\text{\AA}$ and 1450\AA .

Throughout the paper we assume a flat Λ CDM cosmology with $H_0 = 71 \text{ km s}^{-1} \text{ Mpc}^{-1}$, $\Omega_\Lambda = 0.7$ and $\Omega_M = 0.3$. Spectral indices are given assuming $S_\nu \propto \nu^{-\alpha}$.

2. Blazars versus misaligned sources: a test for obscuration

In the simplest version of the Unified Model (e.g. Antonucci 1993; Urry & Padovani 1995; Netzer 2015), QSO are axis-symmetric sources that may appear either absorbed (type 2) or unabsorbed (type 1) depending on whether the line-of-sight intercepts an obscuring structure called dusty torus. In this picture,

the aperture of the dusty torus determines the observed fraction of absorbed QSO in a given sample. Knowing the torus aperture is therefore fundamental in order to account for the (unobserved) obscured population and to obtain a reliable census of the entire population.

The presence of relativistic jets in a fraction of QSO greatly helps to infer the source orientation and, therefore, to assess the existence of an obscuring structure at a certain angle from the jet direction. In particular, the relativistic beaming makes oriented sources orders of magnitudes brighter than misaligned objects and, therefore, easily recognizable thanks to their “blazar properties”, like a core-dominated, flat spectrum radio emission, variability and a strong X-ray emission with a flat photon index. Since beaming effects are maximized for angles within $1/\Gamma$ from the jet direction (Γ is the bulk velocity of the jet), a common assumption is that blazars are observed within this angle, although this statement should be considered valid in a statistical sense. We thus call $\Theta_b = 1/\Gamma$ the “blazar angle”. This means that for each observed blazar there should be $4\pi/\Omega_b \sim 2\Gamma^2$ sources with the same intrinsic properties and with a jet randomly oriented, where Ω_b is the solid angle corresponding to Θ_b ¹. Therefore, given the number of blazars observed in a certain volume of Universe, it is possible to infer the total number of sources with the same properties within the same volume. The presence of obscuration at a certain viewing angle, reduces the observed number of misaligned radio-emitting QSO, if we are selecting only unobserved, type 1, sources. The comparison between the predicted and the observed number of jetted type 1 QSO can thus yield direct information on the impact of obscuration in the sample.

Real samples, however, are typically flux-limited and the situation is more complicated since beaming greatly boosts the fluxes of blazars, thus favouring their inclusion in the sample. For this reason, the non-blazar/blazar relative ratio observed in a flux limited survey is, in general, significantly different from $2\Gamma^2$ and depends on several factors, like the survey limit(s) and the shape of the luminosity function (e.g. see discussion in Lister et al. 2019).

Ghisellini & Sbarato (2016) developed a simple method to predict the expected number of misaligned sources in a flux-density limited sample on the basis of the observed fluxes of blazars selected in the same sample. In summary, given a sample with a flux density limit S_{lim} and containing N blazars in a certain redshift interval, we expect to find, at the same flux limit and within the same redshift interval, a number (N_{tot}) of blazars plus non-blazars (i.e. with a misaligned jet) given by²:

$$N_{tot} \sim \sum_{i=1}^N \left[2 \left(\frac{S_i}{S_{lim}} \right)^{1/p} - 1 \right] \quad (1)$$

where the sum is done on all the blazars selected in the survey and S_i are their flux densities. The parameter “ p ” appears in the beaming model and depends on the jet: for instance, if α is the radio spectral index of the emitting source, we expect $p=3+\alpha$ for a moving, isotropic source and $p=2+\alpha$ for a continuous jet (see Appendix B of Urry & Padovani 1995 review paper for more details). It is worth noting that equation 1 does not depend on the value of Γ , the only free parameter being p . This greatly reduces the uncertainties of the method.

¹ The solid angle corresponding to Θ_b is $2\pi(1-\cos\Theta_b)$. Since jets are emitted along two opposite directions, Ω_b is 2 times this value i.e. $\Omega_b = 4\pi(1 - \cos\Theta_b) \sim 2\pi/\Gamma^2$ (valid for small angles).

² We note that in Ghisellini & Sbarato (2016) this number is wrongly given as the ratio between N_{tot} and the number of blazars (their eq. 8).

We tested the validity of equation 1 via Monte-Carlo simulations and found that it systematically over-predicts the number of sources by a factor ~ 1.4 (see Appendix A). This is likely related to the fact that in the Ghisellini & Sbarro (2016) work all blazars are assumed to be observed at an angle exactly equal to $1/\Gamma$ rather than $\leq 1/\Gamma$. If we take this effect into account, and assume that blazars are observed at different angles within $1/\Gamma$, equation 1 becomes (see Appendix A for its derivation):

$$N_{tot} \sim \sum_{i=1}^N [1.44 \left(\frac{S_i}{S_{lim}}\right)^{1/p} - 1] \quad (2)$$

We will use this formula throughout the paper.

Strictly speaking, the value of N_{tot} provided by equation 2 should be considered as a lower limit on the expected number of jetted high- z QSO since it is computed only on the basis of the jet luminosity, neglecting the un-beamed, extended emission of the source (like that from the radio lobes). This effect can be particularly relevant when working with samples selected at low frequencies where the extended emission is expected to be more important, while it should progressively become less relevant when moving to higher frequencies. When dealing with high redshift ($z > 4$) sources, where a typical observed frequency of 1.4 GHz corresponds to rest-frame frequencies above 7 GHz, the relevance of the extended components should be marginal. In addition, the extended radio emission is expected to be partially dumped by the interaction between the electrons in the jets and the photons from the Cosmic Microwave Background (CMB, e.g. Ghisellini & Tavecchio 2009; Paliya et al. 2020; Ighina et al. 2021). In any case, in the analysis described in the next sections we will always use the peak flux densities, rather than the total integrated flux densities, in order to minimize the possible contribution from any extended emission.

Having derived and tested a method to estimate the expected number of type 1 jetted QSO in a radio flux-limited sample, we can apply it to real samples to see if this number is consistent with the observations. A deficit of the observed number may suggest the presence of obscuration at a given angle from the jet direction. If the sample is large enough, we can even apply equation 2 at different flux densities. In this way it is also possible to infer the angle at which the obscuration occurs, as it will be shown in the next sections.

We first apply the method to the CLASS sample, characterized by a high radio flux limit compared to the optical one. We then build a much radio deeper sample that contains more misaligned objects, making the comparison between predictions and observations more stringent.

3. The CLASS sample

The first sample considered is the CLASS sample of high- z QSO (Caccianiga et al. 2019, Ighina et al. 2019). This is a completely identified flux limited sample of flat-spectrum sources with $z \geq 4$ at the radio limit of 30 mJy at 5 GHz and $\text{mag}_{drop} \leq 21$, covering 13120 sq. degrees of sky at high Galactic latitude ($|b^II| > 20^\circ$). The original complete sample presented in Caccianiga et al. (2019) contained 21 spectroscopically confirmed $z > 4$ QSO, out of which 18 were classified as blazars on the basis of their X-ray emission (see Ighina et al. 2019 and the Section 4.1 for more details on the classification method). The CLASS sample has been used to obtain an accurate estimate of the space density of high- z blazars (Caccianiga et al. 2019; Ighina et al. 2021) and to track

the evolution of the most massive SMBH (above $10^9 M_\odot$) hosted by jetted QSO up to $z \sim 6$ (Diana et al. 2022).

We now add two sources (J222032.5+002537 at $z=4.1960$ and HZQJ142048.0+120546 at $z=4.0344$), both classified as blazars (Sbarro et al. 2015), that were not originally included because their radio spectrum between 1.4 and 5GHz was steeper than 0.5 and, therefore, above the threshold used to define CLASS ($\alpha_R \leq 0.5$)³. Therefore, the final sample considered here contains 23 sources, 20 classified as blazars and 3 as misaligned objects (see Tab. C.1). At first glance, this dominance of blazars in the CLASS sample could be considered as an evidence of the fact that obscuration plays an important role in hiding misaligned sources. However, as previously discussed, the actual fraction of blazars in a flux limited sample depends on several factors and only using the method described in Section 2 we can establish whether the observed number is consistent or not with the expectations.

If we apply equation 2, where $N=20$ is the total number of blazars and S_i are their 5 GHz flux densities reported in Tab C.1 (column 7), we predict the existence of 20-24 QSO (using $p=3$ and 2 respectively) in the same area and with the same radio and magnitude limits, that is 5 misaligned sources at most. This is fully consistent with what we observe. Therefore, the large fraction of blazars observed in the CLASS survey is not surprising, and it is simply due to the high radio flux limit compared to the optical one, something that favours the selection of sources with high radio-to-optical flux ratio i.e. oriented sources.

The fact that CLASS is not very sensitive to sources observed at large viewing angles implies that we are only able to test the presence of obscuration at angles slightly above $1/\Gamma$. In order to extend the test at large angles, it is necessary to lower the radio flux limit, while keeping the same optical limit. In this way, we will start selecting more sources with lower radio-to-optical flux ratio values that are likely observed at larger viewing angles. In the next section, we discuss the selection of a sample that is much deeper in the radio than CLASS (by more than a factor 10) but has the same optical limit.

4. The FIRST sample

In order to extend the analysis at lower flux densities, we have considered the sample of $z > 4$ QSO detected in the FIRST catalogue (Becker et al. 1995). The sample was selected by cross-matching FIRST sources with all the objects in the SDSS-DR17 database spectroscopically classified as "QSO" with $z \geq 4$, using the provided spectroscopic search tool⁴. We then complemented this search by considering all the known QSO from the literature with a spectroscopically confirmed redshift above 4, using either NASA/IPAC Extragalactic Database⁵ or SIMBAD⁶. To obtain a reliable quantification of the number of $z > 4$ QSO we restricted our analysis to a specific sky area ($9h \leq RA \leq 16h$, $0^\circ \leq DEC \leq 60^\circ$, $|b| > 20^\circ$) where we expect that most of the $z \geq 4$ and $\text{mag}_{drop} \leq 21$ have been actually identified thanks to the SDSS spectroscopy. We have verified that in this area, that covers 5215 sq. degrees, all the high- z sources with $\text{mag} \leq 21$ present

³ These objects are the only known $z > 4$ QSO in the sky area covered by CLASS with a flux density at 5 GHz above 30 mJy. In principle, there could be more sources not yet discovered as high- z QSO. However, most of the high- z QSO in the northern sky and with $\text{mag} \leq 21$ should have been already found, thanks to the Sloan Digital Sky Survey (SDSS) spectral database (see also discussion in Section 4).

⁴ <https://skyserver.sdss.org/dr17/SearchTools/SQS>

⁵ <http://ned.ipac.caltech.edu/>

⁶ <http://simbad.cds.unistra.fr/simbad/>

in CLASS have an SDSS spectrum in the last data release. For this reason, we are confident that the completeness of the sample is high ($>90\%$), at least up to $z\sim 5.5$. This is in agreement with the results from Schindler et al. (2017) showing that in this sky area and for relatively faint magnitudes (>19) the QSO selection should be highly complete.

The SDSS spectra of all the $z>4$ QSO from DR17 falling in this sky area have been visually inspected in order to confirm the redshift or exclude objects with a wrong z estimate (most of which claimed to be at $z>5$). In addition, we have searched for all the sources in the literature that have been classified as $z\geq 4$ QSO (with a spectroscopic observation) in the same sky area. We have thus obtained a list of 1330 spectroscopically confirmed $z\geq 4$ QSO with $\text{mag}_{\text{drop}} \leq 21$, 66 of which are detected in the FIRST catalogue ($S_{1.4\text{GHz}}^{\text{peak}} > 1$ mJy). Sixty-two of these objects have a spectrum from SDSS, while 4 sources have been found from the literature (see Tab. C.1). Two of these (J090132.6+161506 at $z=5.63$, Bañados et al. 2015 and J112925.3+184624 at $z=6.82$, Banados et al. 2021) are at $z>5.5$ where the completeness of the SDSS is known to be lower. The other two objects (J101337.8+351849, Gloude-mans et al. 2022 and J145224.2+335424, Stern et al. 2000) have redshift below 5.5. Overall, the sources that are not found by the SDSS represent $\sim 6\%$ of the sample ($\sim 3\%$ considering the $4\leq z\leq 5.5$ range) and this is consistent with the hypothesis that the SDSS spectroscopic sample is highly complete ($>90\%$) in this area of sky and for sources in this range of redshift and magnitude.

Since the FIRST catalogue has been produced using a $5\times\text{rms}$ threshold, it is possible to extend the sample down to lower flux densities using the FIRST radio data and searching for $S_{1.4\text{GHz}}^{\text{peak}} \geq 0.5$ mJy/beam ($>3\times\text{rms}$) around the optical position of $z>4$ QSO. This lower threshold is reasonable considering that we are "forcing" the photometry towards a limited number of known positions and not carrying out a blind search, as the original FIRST catalogue. Using this technique, we have found 7 additional sources with peak surface densities between 0.5 and 0.9 mJy/beam. One of these sources (J133422.6+475033) has been also detected at 140 MHz in the Low Frequency Array (LOFAR) Two-metre Sky Survey (LoTSS, Gloude-mans et al. 2022). The radio maps of these newly discovered radio detections are reported in Fig.1. Since it is difficult to test the actual completeness of this extension at 0.5 mJy we use the original sample at 1 mJy for most of the computations while we use the extension only to reveal hints of possible trends at lower flux densities.

In total, the final FIRST sample contains 73 $z\geq 4$ radio-emitting QSO with a peak flux density at 1.4 GHz ≥ 0.5 mJy/beam and $\text{mag}_{\text{drop}} \leq 21$. In Tab.C.1 these sources are flagged with the letter "F". These 73 radio detections correspond to 5% of the total number of $z\geq 4$ type 1 QSO with $\text{mag}\leq 21$ present in the considered sky area (1330).

Nine sources in the FIRST sample are in common with CLASS (i.e. all the CLASS high- z QSO falling in the sky area covered by FIRST). Therefore, the two samples studied here contain a total of 87 independent $z\geq 4$ jetted QSO.

4.1. Blazar classification

In order to apply eq. 2 it is necessary to recognize all blazars present in the FIRST sample. Historically, blazars with emission lines were identified with the class of FSRQ that are defined on the basis of their flat ($\alpha_R < 0.5$) radio spectrum. A flat spectrum is usually attributed to a source that is dominated by the self-absorbed emission from the core, i.e. from the relativis-

tically boosted, unresolved part of the jet (e.g. Urry & Padovani 1995). Often, the slope of the radio spectrum is evaluated on the basis of non-simultaneous flux densities measured at two different frequencies. Not only variability may affect the measure of the slope, but also complex spectral shapes, like peaked spectra, can lead to a mis-classification of a source as FSRQ if only two points are used to characterize the spectrum. This is particularly true for high- z jetted QSO that often show gigahertz-peaked spectra, possibly due to their young age (e.g. Frey et al. 2011; Momjian et al. 2021; Zhang et al. 2021; Belladitta et al. 2023). Moreover, at high redshifts we usually observe at high rest-frame frequencies where the core, that has a flat spectrum, can dominate over the steep-spectrum extended emission even in moderately mis-aligned sources. This can be even more true considering that the extended emission can be dumped at high redshift due to the effect of the CMB, as mentioned in Sect. 2. For all these reasons, while the two-points radio spectrum can be effectively used to efficiently pre-select high- z blazar candidates (e.g. Caccianiga et al. 2019), caution should be used in adopting the radio slope to classify a source, in particular when the spectrum is measured with non-simultaneous flux densities. The availability, in the next future, of surveys like GLEAM-X (Wayth et al. 2018; Hurley-Walker et al. 2022) that will provide simultaneous spectra between 72 and 231 MHz (corresponding to rest-frame frequencies of 400MHz-1.3GHz at $z=4.5$) for sources down to 5 mJy, will allow a more accurate spectral classification of high- z radio-emitting QSO.

Alternatively (or in addition), high-resolution, VLBI observations are often used to constrain the orientation of a high- z QSO. In particular, the detection of a high brightness temperature (T_b) above the equipartition limit, is usually considered a robust way to classify a source as blazar (Frey et al. 2008, 2010; Gabanyi et al. 2015; Coppejans et al. 2016; Frey et al. 2018; Spingola et al. 2020; Liu et al. 2022; Krezinger et al. 2022). Unfortunately, for sources of a few mJy (or below) the maximum baseline available on earth is not long enough to put a stringent limit on T_b able to unambiguously classify a source as blazar. Also, the sensitivity could be an issue for very faint sources. Even for brighter objects, the estimate of T_b requires an accurate measure of the source size that is often only a small fraction of the synthesized beam, and this may be a challenging task. Finally, the systematic follow-up with VLBI techniques of large samples of high- z QSO can be particularly time-consuming.

A third method to classify a source as blazar is based on the analysis of the Spectral Energy Distribution (SED). A SED showing a strong and "rising" X-ray emission (e.g. with a Photon index below 1.5), well above the one expected for a non-jetted QSO, due to the electrons of the hot-corona, is considered a clear signature of the orientation of the source (Ghisellini et al. 2010; Sbarrato et al. 2012, 2013b; Ghisellini et al. 2019; Sbarrato et al. 2021, 2022). In Ighina et al. (2019) we have used a similar method, based on the X-ray-to-optical luminosity ratio, parametrized by the $\tilde{\alpha}_{ox}$ index⁷, and on the X-ray spectral slope to quantify the X-ray dominance in the SED and to easily distinguish blazars from mis-aligned sources. If the X-ray spectral index is not available, or poorly determined, the $\tilde{\alpha}_{ox}$ parameter alone can be effectively used.

The different methods described above do not always agree in classifying the sources (e.g. see discussion in Krezinger et al.

⁷ According to Ighina et al. (2019) we define $\tilde{\alpha}_{ox} = -\frac{\log(L_{10\text{keV}}/L_{2500\text{\AA}})}{\log(\nu_{10\text{keV}}/\nu_{2500\text{\AA}})} = -0.3026 \log\left(\frac{L_{10\text{keV}}}{L_{2500\text{\AA}}}\right)$, where $L_{10\text{keV}}$ and $L_{2500\text{\AA}}$ are, respectively, the X-ray and UV monochromatic luminosities (per unit of frequency) Blazars are characterized by $\tilde{\alpha}_{ox} \leq 1.355$.

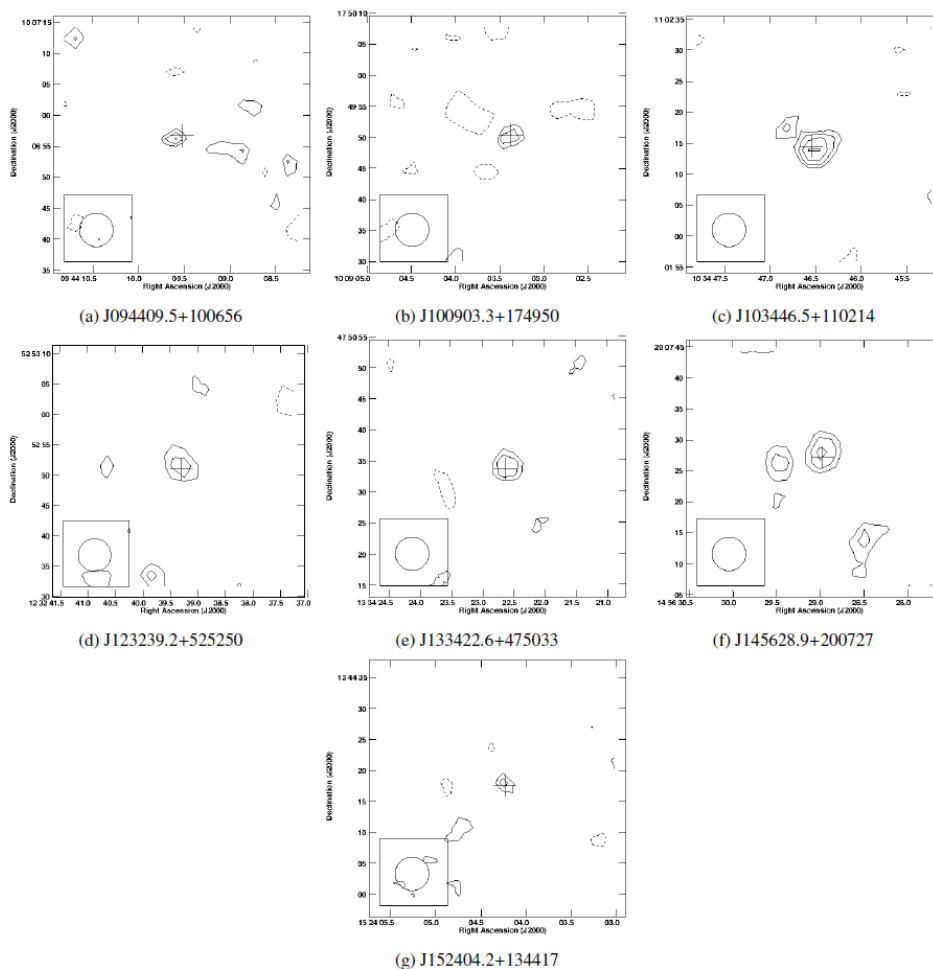


Fig. 1: Radio maps at 1.4 GHz from FIRST data of the 7 high- z QSO in the sample with peak flux densities between 0.5 and 0.9 mJy/beam, not included in the FIRST catalogue. Levels are computed as $-2, 2, 2.8, 4, 5.5, 8, \dots$ times the rms (0.15 mJy/beam). The beam size is indicated in the bottom-left corner.

2022) and it is likely that the most reliable classification for a single object will be achievable only by combining all the pieces of information available from radio to X-rays. For large samples, however, using a single method like the one based on X-ray data can represent a reasonable compromise to easily obtain a uniform classification that is sufficiently reliable, at least from a statistical point of view. For this reason, we adopt the X-ray method to classify the sources in the FIRST sample. This is the same method adopted for the CLASS sample as explained in the previous section and in Ighina et al. (2019). In Appendix B we discuss the reliability of the adopted classifications by comparing them with those based on SED modelling and VLBI data from the literature. In Sect. 4.2 we will evaluate the impact of possible mis-classifications on the final results.

For radio flux densities above 30 mJy nearly all sources are included in the CLASS sample of high- z QSO and, therefore, we can use the classifications obtained in Ighina et al. (2019). For lower flux densities, we expect a smaller number of blazars since the average radio-to-optical flux ratio decreases progressively when lowering the radio flux density limit and keeping the same optical limit. In order to apply the same criteria used in Ighina et al. (2019) to classify the sources in the FIRST sample, we exploited all the available sources catalogues of the major existing X-ray telescopes (*XMM-Newton*, *Chandra*, *Swift-XRT*, *NuSTAR*). This search has provided X-ray data for 24 objects.

In particular, for 18 sources we have fluxes from the Chandra Source Catalog Release 2.0 (CSC 2.0, Evans et al. 2010) and for 6 additional objects we have obtained an X-ray flux from Swift XRT Point Source Catalogue (2XSPS, Evans et al. 2020). The Chandra 0.5–7.0 keV fluxes, computed using a power-law with a fixed photon index of 2.0, and the Swift-XRT 0.3–10 keV fluxes, computed assuming a power-law with a fixed photon-index of 1.7, all corrected for the Galactic absorption, are then converted into the rest frame monochromatic 10 keV flux assuming the same photon indices mentioned above. The $\tilde{\alpha}_{ox}$ is finally derived by combining the computed X-ray flux at 10 keV and the monochromatic flux at 2500Å (rest frame) estimated from the z magnitude and using the optical spectral index computed between WISE W1 and z magnitudes, if available, or assuming $\alpha_o=0.44$ (Vanden Berk et al. 2001).

For one additional object (J091316.5+591921), not present in the two catalogues mentioned above, we have derived the value of $\tilde{\alpha}_{ox}$ from the α_{ox} (defined between 2500Å and 2 keV) published in Wu et al. (2013) and using the conversion formula reported in Ighina et al. (2019). For one more object (J090132.6+161506) we have analyzed a 13ks public Chandra observation (PI: Garmire) and computed the X-ray flux. Finally, for 2 additional sources, not included in the CSC2.0 and 2XSPS catalogues but for which there is a Chandra or Swift-XRT ob-

servation, we have derived an upper-limit on the X-ray flux and, consequently, a lower limit on $\tilde{\alpha}_{ox}$.

In total, we have obtained X-ray data for 28 objects that represent 38% of the sample (see C.1). The fraction of sources without a classification is therefore quite high (62%). It should be noted, however, that not all the sources without X-ray data are reasonable blazar candidates. Blazars are typically characterized by high radio-to-optical luminosity ratios. We quantify the radio-to-optical relative strength of a source adopting the commonly used radio-loudness parameter (R) defined as (Kellermann et al. 1989): $R = \frac{S_R}{S_O}$, where S_R and S_O are the k-corrected flux densities at the rest-frame frequency 5 GHz and 6.81×10^{14} Hz respectively (corresponding to a wavelength of 4400 Å). Typically, blazars have high radio-loudness values ($\gtrsim 100$ e.g. Sbarrato et al. 2015). Indeed, considering all the $z \geq 4$ QSO currently detected at radio wavelengths and with a classification based on X-ray data, we notice that the large majority (93%) of the sources with $R \geq 1000$ are classified as blazars on the basis of the X-rays. Vice versa, only $\sim 15\%$ of the sources with $R < 80$ have values of $\tilde{\alpha}_{ox}$ consistent with those of blazars (most of which close to the 1.355 threshold). In the intermediate region ($80 \leq R < 1000$) we have a mix of possible classifications. This means that, if X-ray data are missing, only sources with a radio-loudness between 80 and 1000 really need to be observed while the remaining sources can be classified as blazars or non blazars only on the basis of their radio-loudness (at least with a $\sim 90\%$ confidence level). Out of the 45 objects in the FIRST sample without X-ray data, only 10 have $80 \leq R < 1000$ while the remaining have $R < 80$. We have a running project aimed at observing these 10 sources with Swift-XRT. More X-ray observations will be available when data from the ongoing *eROSITA* all-sky survey (Merloni et al. 2012) will be released. For the time being, we will estimate the impact of the sources with missing classification to the final results (Sect. 4.2).

Table C.1 summarizes the properties of all the sources in the sample including, when available, a classification as blazar/non-blazar based on X-ray data. In particular, 20 sources have been classified as blazars in the FIRST sample. Since nine of these sources are in common with the CLASS sample, Table C.1 contains a total of 31 high- z QSO classified as blazars.

4.2. Results

We can now apply equation 2 to the blazars selected in the FIRST sample to predict the expected number of radio-emitting high- z QSO. In Fig. 2 we show the expected number of sources with a peak flux density above 1 mJy as a function of the parameter "p", which is the only free parameter in equation 2. We obtain a number consistent with the one observed for a reasonable value of p (~ 3.3) with a [2.9-4.0] 2σ interval. Considering that the average spectral index of the sample is $\sim 0.1-0.4$, depending on the frequencies, the value of $p=3.3$ is consistent with the scenario of a moving, isotropic source ($p=3+\alpha$, Urry & Padovani 1995). We note that the inclusion of the unclassified sources as blazars in the analysis would increase the derived value of p. If we consider as blazars all the objects without X-ray data but with a radio-loudness higher than 80 (see discussion in the previous section) we obtain a value of p of 3.8. This is an extreme case, since we do not expect that all these objects are blazars. Also, the possible misclassifications can have an impact on the best-fit value. If we exclude all blazars whose classification is not supported by VLBI data (see Appendix B) we obtain a slightly lower value of p (3.0). Realistically, the actual value of p should

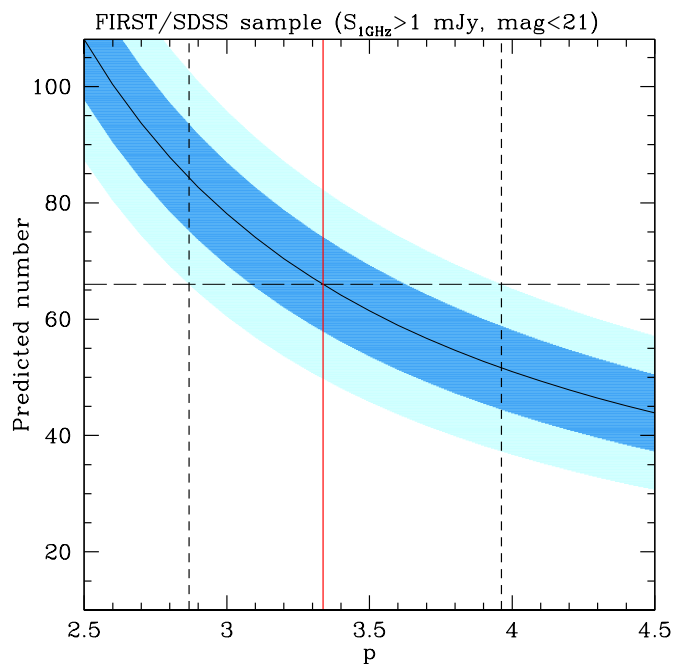


Fig. 2: Predicted number of $z \geq 4$ QSO (both blazars and non-blazars) with flux density at 1.4 GHz ≥ 1 mJy and $\text{mag}_{drop} \leq 21$ in the sky area covered by the FIRST sample, based on the observed number of blazars in the same area. The predictions are shown as a function of the parameter "p" while the shaded area shows the Poissonian uncertainty on this number (dark blue = 1σ , light blue = 2σ). The horizontal dashed line indicates the observed number of sources, while the vertical lines report the best value of p (red solid line) together with the 2σ confidence interval (black short-dashed lines).

be included between 3 and 3.8. Since all these values of p are reasonable, we conclude that no significant departures from the beaming model expectation are observed, even considering the uncertainties related to the delicate issue of the blazar classification.

Another way of applying eq 2 is to split the sample at different flux limits and predict the expected number of jetted sources at each flux density. In this way, we do not just compare the total predicted number of sources with the observed one, but we also test the distribution of the numbers as a function of the flux limit. In addition, if we are confident that no - or very few - blazars with $\text{mag}_{drop} \leq 21$ are present at flux densities below the FIRST limit, we can even extrapolate this computation to very flux densities since the presence of blazars at higher flux densities implies the existence of well-defined numbers of misaligned objects at much lower flux densities. This is shown in figure 3 where we have assumed the best-fit value $p=3.3$. In this figure, we have quantified the impact of the sources without a classification as blazar or non-blazar by assuming the extreme scenario in which all the unclassified sources with a radio-loudness above 80 are blazars: this corresponds to the upper part of the light-blue area reported in the figure. Realistically, the correct curve should fall within the blue shaded area, probably closer to the lowest line (corresponding to the case where no blazars are present among the unclassified objects). We have also evaluated the impact of the blazar classifications that are not confirmed by VLBI data (see Appendix B) by excluding them from the analysis (dashed line)

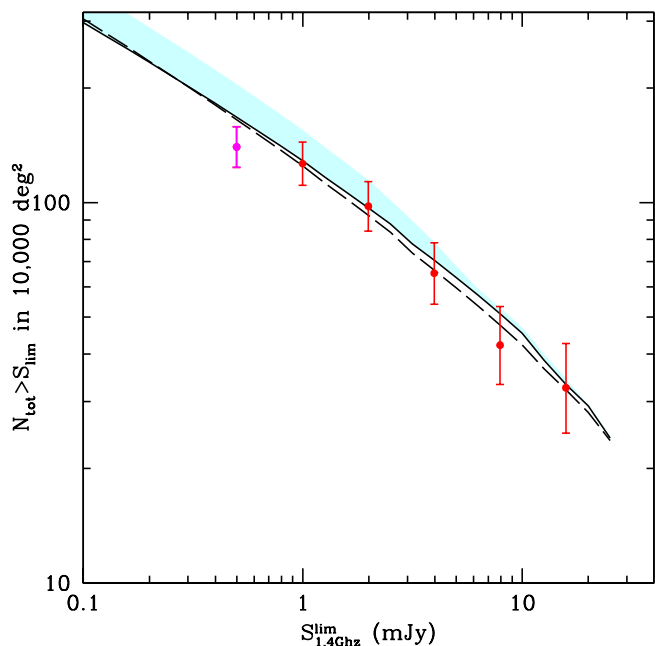


Fig. 3: Predicted number, on a sky area of 10 000 sq. degrees, of $z \geq 4$ jetted type 1 QSO (blazars+mis-aligned sources) with $\text{mag}_{\text{drop}} \leq 21$ for different radio flux density limits, based on the high- z blazars currently detected at 1.4 GHz in the FIRST sample (mostly at flux densities above 10 mJy) described in the text. The predictions (black solid line) assume the best value of p (3.3). The light-blue shaded area indicates the possible impact of the sources with missing classification under the (extreme) assumption that all the sources missing X-ray data and with a radio-loudness above 80 are blazars. The dashed line, instead, shows the impact of the mis-classifications: the line is computed by excluding all blazars that are not confirmed by VLBI observation (see Appendix B). In this case, we assume $p=3.0$. Red points represent the observed sources from the FIRST catalogue while the magenta point indicates the extension down to 0.5 mJy/beam based on FIRST maps.

and assuming $p=3.0$. As clear from the figure, the impact of the possible mis-classifications is marginal.

Overall, the shape of the distribution seems in good agreement with the predictions, considering the statistical errors, although the last point, at 0.5 mJy, suggests a possible flattening of the curve. This hint of flattening, however, is statistically marginal, and it could be related to some incompleteness of our extension of the FIRST catalogue below 1 mJy. More data are required in order to confirm this possible trend.

In case of a significant deficit of sources observed at low flux densities, compared to the predictions, it will be possible to infer the presence of an obscuring structure and to quantify its angular aperture. For instance, according to the AGN Unified Model we expect that above a certain viewing angle the line-of-sight will intercept the molecular torus that will obscure the innermost QSO emission like that from the Broad Line Region (BLR) and the accretion disk. The consequence will be a progressive paucity of observed type 1 QSO (the class of sources that we are considering here) as we move towards lower radio flux densities, where sources are observed - on average - at larger angles.

If we take into account this effect, we expect a flattening of the number of jetted (type 1) QSO below a critical flux density

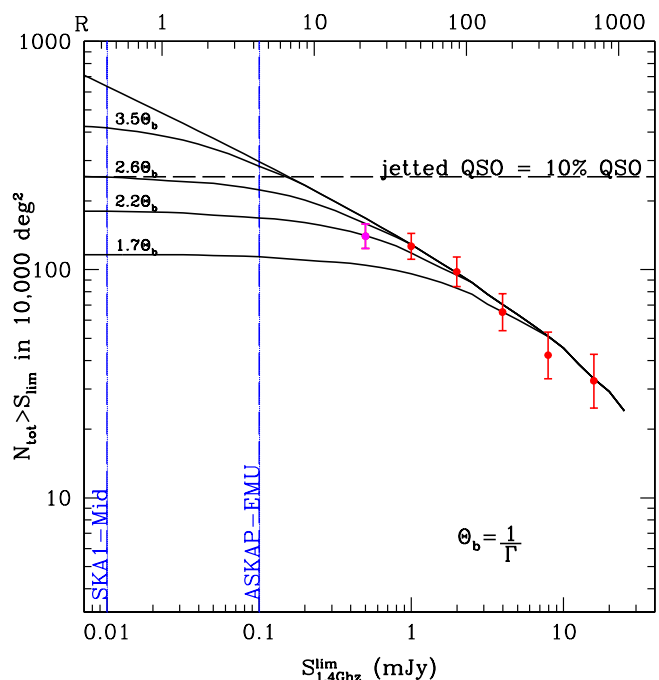


Fig. 4: As figure 3 but showing the impact of a circumnuclear obscuring torus with different aperture angles expressed in units of beaming angle $\Theta_b = 1/\Gamma$ (the uppermost line represents the case of no-absorption). The upper scale of the figure shows the representative values of radio-loudness (R) corresponding to the flux density limit in the X-axis and using a magnitude of 21 and assuming an average redshift of 4.5. The depth ($5 \times \text{rms}$) of some ongoing/planned surveys is also indicated. Points as in previous figure. The horizontal dashed line indicates the expected total number of jetted QSO in 10,000 sq. degrees if they represent 10% of the total QSO population.

that depends on the torus aperture. We note that, while the number of jetted QSO predicted according to the equation 2 does not depend on the Lorentz factor, the flux density limit at which we expect the flattening does. Indeed, for a given torus critical aperture, the corresponding observed flux density depends on the jet bulk velocity: for larger (lower) values of Γ the break on the number density will be observed at lower (larger) flux densities. In Fig. 4 we report the expected number of jetted type 1 QSO at $z \geq 4$ and $\text{mag}_{\text{drop}} \leq 21$ in a sky area of 10000 sq. degrees at different flux density limits considering different torus apertures expressed in units of “blazar” angle $\Theta_b = 1/\Gamma$.

Assuming that there are no blazars among the unclassified sources, the data points currently do not suggest the presence of a significant level of obscuration at angles lower than ~ 2 times the critical angle Θ_b i.e. below $10\text{-}20^\circ$, for $\Gamma=10\text{-}5$ respectively. The detection of some new blazars among the unclassified source may increase the discrepancy between the point at 0.5 mJy and the predictions, although, as explained above, this point may suffer from some incompleteness. Deeper radio surveys are necessary to better quantify the number of sources at flux densities below 1 mJy and to extend this test to even lower fluxes, corresponding to larger viewing angles (see Sect. 5).

4.3. Fraction of jetted QSO and absorption

Since we built the FIRST sample on a sky area where the total number of $z \geq 4$ QSO (both radio-quiet and radio-loud) with

$\text{mag}_{\text{drop}} \leq 21$ is known, mostly thanks to the SDSS spectroscopic archive, it is possible to estimate the fraction of jetted QSO at these redshifts.

The LogN-LogS presented in Fig. 4 is expected to converge, at very low flux densities, to the total number of jetted QSO i.e. $2\Gamma^2 \times N_{\text{blazar}}$ (see discussion in Sect. 2). Since we are dealing only with un-obscured sources, the actual number is:

$$2\Gamma^2 \times N_{\text{blazar}} \times (1 - f_{\text{obsc}})$$

where f_{obsc} is the fraction of obscured sources ($N_{\text{obsc}}/N_{\text{tot}}$). Therefore, the existence of 20 blazars in this area and with $\text{mag}_{\text{drop}} \leq 21$ implies the existence of $\sim(1000-4000) \times (1 - f_{\text{obsc}})$ jetted type 1 QSO with the same optical limit, using $\Gamma=5-10$ respectively. If we assume that the fraction of obscured (type 2) jetted QSO is similar to that proposed for the total QSO population ($\sim 70\%$, Vito et al. 2018) we expect, in this sky area, 300-1200 jetted type 1 QSO, most of which not detectable in the existing radio surveys due to their very low radio flux. In the same area of sky we have counted 1330 $z \geq 4$ QSO, independently to the radio detection (see Sect. 4). Therefore, depending on the actual value of Γ , a significant fraction (23-90% for $\Gamma=5$ and 10 respectively) of QSO at $z \geq 4$ could have a powerful relativistic jet currently not detected because strongly de-beamed. This result is consistent with what has been found by Diana et al. (2022) using blazars in the CLASS survey (see their figure 5) but it is in apparent disagreement (in particular for high Lorentz factors) with the results presented by Liu et al. (2020) who found a radio-loud fraction at $z \sim 6$ close to 10% ($9.4 \pm 5.7\%$). We note, however, that a direct comparison of this number with the fraction of jetted QSO derived above is difficult since our estimate of the fraction of jetted QSO is not based on the value of radio-loudness, as in Liu et al. (2020), who used $R > 10$ to define a QSO as radio-loud. In our estimate, instead, the misaligned jetted QSO that we infer from the observed number of blazars do not necessarily have $R > 10$ since their core emission is expected to be significantly de-beamed at large viewing angles (see Sect. 5.2 for a discussion). And, indeed, seven objects in the FIRST sample have a radio-loudness between 1 and 10. In this sense, the definition of radio-loud QSO has a somewhat ambiguous meaning, in particular when the radio flux is dominated by the core emission which is strongly dependent on orientation (see also the discussion in Sbarrato et al. 2021).

Alternatively, if we assume that the fraction of jetted QSO is similar to what is found in Liu et al. (2020) ($\sim 10\%$) the fraction of obscured sources must be much higher than 70%, of the order of 87%-97%. Therefore, assessing the importance of obscuration in high- z jetted QSO is intimately related to the problem of how ubiquitous powerful relativistic jets were in the primordial Universe.

In order to distinguish between these scenarios (high fraction of jetted QSO or high fraction of obscured QSO) we need to reach low flux densities. In figure 4 we show the case where jetted QSO represent 10% of the total population (dashed horizontal line). This is the value to which the logN-logS should converge at low radio flux densities if the fraction of jetted QSO is really 10%. Reaching flux densities of ~ 0.1 mJy would already allow us to confirm or reject this possibility. This is a feasible task that can be accomplished in the next few years, as discussed in the next section.

5. Predictions at sub-mJy flux densities

Next years will be particularly promising as far as the radio surveys are concerned. Square-Kilometre Array (SKA) precursors

and pathfinders and, subsequently, SKA Observatory (SKAO) itself, are carrying out, or planning, several continuum surveys that will significantly improve the existing ones. From figure 4 it is clear that we need surveys covering a significant portion of the sky (at least a few thousands of sq. degrees, in order to find a sizable number of objects) reaching flux density limits below $100 \mu\text{Jy}/\text{beam}$ where we may expect to see a flattening of the high- z RL QSO number counts. A critical point, when going to such a low flux density level, is that the core emission may not be dominant any more because of the strong de-beaming expected at large viewing angles. The presence of a significant fraction of extended emission⁸ may cause the inclusion in the sample of more sources than expected on the basis of the sole core emission, thus affecting the analysis. Using high frequencies may help to limit but not completely eliminate this problem. Therefore, a good spatial resolution, of less than a few arcsec, will also be very important in order to resolve the source and distinguish the core from the extended emission.

At ~ 1 GHz frequency, a promising survey is the "Evolutionary Map of the Universe" (EMU) that is ongoing at the Australian SKA Pathfinder (ASKAP) radio telescope (Norris et al. 2011, 2021). The survey will cover the sky at declination below $+30^\circ$ with an expected RMS noise level of 20-25 $\mu\text{Jy}/\text{beam}$. Unfortunately, the resolution of EMU is relatively poor ($\sim 12''$) and the separation from core and extended emission may not be always possible. A follow-up of the detected sources could be necessary in order to estimate the correct flux density from the core.

An outstanding improvement, both in sensitivity and angular resolution, will be possible thanks to the wide-field continuum surveys that will be carried out by SKA1-Mid. The continuum sensitivity (RMS in 1 hour) is expected to be 2 $\mu\text{Jy beam}^{-1}$ at 1.4 GHz with a resolution of $0.4''$ (Braun et al. 2019). With this kind of imaging sensitivity and resolution, it will be possible to robustly test the presence of obscuration at large viewing angles.

In Fig. 4 we show the $5 \times \text{rms}$ flux limit of the surveys mentioned above, showing their actual capability of distinguishing between different scenarios. Reaching flux densities of a few tens of μJy should allow us to test the presence of obscuration at angles up to $\sim 30-35^\circ$, where the "standard" obscuring torus should be present.

An important point that should be considered when moving towards such low radio flux densities while keeping the same optical limit is that, at a certain flux level, we start sampling the population of QSO whose radio emission is not powered by a relativistic jet but could be related, for instance, to an intense star-formation. These are the sources usually classified as "radio-quiet" (RQ) on the basis of a low radio-loudness ($R < 1$). While in radio-loud (RL) QSO, with radio-loudness above 10, the presence of a relativistic jet is well established, in RQ QSO the origin of the radio emission is still a matter of debate. In the upper side of Fig. 4 we report the values of radio-loudness computed using the radio flux density limit on the X-axis and the optical flux density at 4400\AA corresponding to $\text{mag}_{\text{drop}}=21$ and assuming $z=4.5$, $\alpha_R=0.1$ ⁹ and $\alpha_O=0.44$ (Vanden Berk et al. 2001). This scale gives an approximate indication of the typical

⁸ It is however possible that extended emission in the early Universe was strongly damped due to the interaction with the CMB, as mentioned in Sect. 2.

⁹ $\alpha_R=0.1$ is the average spectral slope measured for the sources in the sample between 144/150MHz and 1.4 GHz using data from LoTSS (Shimwell et al. 2022) and TGSS (Intema et al. 2017). These indices are reported in Tab. C.1

values of R expected at each radio flux limit. For instance, among the 73 sources in the FIRST sample discussed here, the majority (65) have $R > 10$ in the typical range of RL QSO, the remaining having R between 1 and 10. In the deeper ongoing/planned surveys, like ASKAP-EMU, instead, we should expect a significant fraction of sources with R between 1 and 10 or even below 1. The sample based on the very deep SKA1-Mid surveys will be almost completely made up by objects with a value of R in the RQ range (< 1). This is interesting since the simple discovery of high- z blazars at high flux densities (> 10 mJy) implies the existence of many misaligned jetted high- z QSO well in the “RQ regime” (the actual number depending on the importance of the extended emission as explained above). Recent results by Sbarrato et al. (2021) suggest that some high- z QSO with a radio-loudness well below the RL/RQ threshold do actually show evidence for the presence of a misaligned jet, putting into question the simple use of the radio-loudness parameter to discriminate between jetted and non-jetted QSO, at least in this range of redshift.

In any case, the overlap between misaligned jetted QSO and non-jetted QSO, whose radio emission could be due to star-formation or other mechanisms, is a potential issue since the possible inclusion of non-jetted QSO in the plot shown in Fig. 4 is expected to produce a steepening of the curve below a certain flux limit thus affecting the final results. In principle, it should be possible to distinguish between the two classes of sources by studying the radio morphology (at arcsec and sub-arcsecond scales) as demonstrated by Sbarrato et al. (2021) or using the value of Brightness Temperature measured in high resolution radio images (see e.g. Morabito et al. 2022). In this context, wide-field VLBI surveys would be ideal to assess the presence of a jet (e.g. Radcliffe et al. 2021). Also, the observed radio luminosity can be used to distinguish QSO whose radio emission is powered by a jet from those powered by star-formation. For example, all the sources in the FIRST sample with a radio-loudness parameter between 1 and 10 have radio powers at 1.4 GHz between 10^{26} and 10^{27} W Hz $^{-1}$ i.e. well within the typical range of power observed in jetted QSO, in spite of their relatively low radio-loudness values.

6. Conclusions

We have discussed and further developed a method, firstly proposed by Ghisellini & Sbarrato (2016), to evaluate the presence of obscuration in jetted QSO in the early Universe ($z \geq 4$), based on the number of blazars observed in a flux limited sample. We have applied this method to two well-defined samples of high- z type 1 jetted QSO containing, in total, 87 independent $z \geq 4$ radio-emitting QSO, including 31 sources classified as blazars on the basis of the X-ray emission.

The first sample (the CLASS high- z sample), containing 23 sources, is characterized by a high radio flux density limit (30 mJy at 5 GHz) while the second one is based on the combination of the last data-release of SDSS (DR17) and FIRST and contains 73 sources (9 sources are in common with the CLASS sample). This sample has a much deeper radio limit (0.5 mJy) compared to CLASS but it has the same optical limit ($\text{mag}_{\text{drop}}=21$).

The main results can be summarized as follows:

- In the CLASS sample, blazars represent the large majority ($\sim 85\%$) of the sources, with only a small fraction of misaligned objects. Our analysis shows that this dominance of oriented sources is consistent with the predictions of the beaming model and, therefore, it is likely due to the high

radio-to-optical flux limit ratio of the CLASS sample that favours the selection of oriented sources, and it is not caused by the obscuration along large lines-of-sight;

- Using the FIRST sample which contains a larger fraction of misaligned sources compared to CLASS we do not observe any significant departure from the beaming model predictions, although a possible deviation is hinted at low flux densities (~ 0.5 mJy). It is possible, however, that this suggested trend is simply due to the incompleteness of the FIRST survey at such low flux density limit;
- Since a reliable blazar/non-blazar classification based on X-ray data is only present for the radio brightest sources in the FIRST samples (i.e. for $\sim 40\%$ of the objects) we cannot exclude that a discrepancy may appear once all the sources in the sample are correctly classified. However, considering that only sources with a relatively high radio-loudness are reasonable blazar candidates, the impact of the unclassified sources is quite marginal. Swift-XRT observations of the objects in the sample with the highest radio-loudness are in progress. In addition, the first data release of the *eROSITA* All Sky Survey (Merloni et al. 2012), expected in the next months, will certainly help to classify the sources since even a non-detection can be used to exclude their blazar nature;
- Next generation radio surveys, like ASKAP EMU and, eventually, those carried out with SKA1-Mid, will be able to sample much deeper radio limits and, therefore, much larger observing angles compared to the existing surveys. At some point, we do expect to observe a significant departure from the predictions, due to the presence of the “standard” obscuring torus. At these very low flux densities (tens of μJy), however, distinguishing between misaligned QSO and RQ QSO, i.e. sources not powered by a radio jet, could be challenging as the radio-loudness parameter will no longer be expected to be useful in separating the two types of sources. High resolution radio follow-up will be instrumental to distinguish the two classes of AGNs. Another critical point will be separating the core emission from that coming from isotropic extended structures, since at large observing angles the former will become less relevant. Again, using data with good resolution and at the highest possible frequency will be fundamental for a reliable analysis.

Assessing the fraction of optically absorbed jetted high- z QSO is also fundamental to establish how common powerful relativistic jets were in the early Universe. If the fraction of optically absorbed sources is similar to that estimated in high- z radio-quiet QSO ($\sim 70\%$) the number of jetted QSO could be much higher compared to the local Universe, representing up to 90% of the QSO population. Conversely, if jetted QSO represent only $\sim 10\%$ of the total population, as in the local Universe, the fraction of obscured jetted QSO could be much higher than expected, between 87% and 97%. Deep radio surveys will be instrumental to distinguish between these two possible (and intriguing) scenarios.

Acknowledgements. We acknowledge financial contribution from the agreement ASI-INAF n. I/037/12/0 and n. 2017-14-H.0 and from INAF under PRIN SKA/CTA FORECaST. We acknowledge financial support from INAF under the project “QSO jets in the early Universe”, Ricerca Fondamentale 2022 and under the project “Testing the obscuration in the Early Universe”, Ricerca Fondamentale 2023. CS acknowledges financial support from INAF (Grants 1.05.12.04.04). This work has been partially supported by the ASI-INAF program I/004/11/4. This work is based on FIRST and SDSS data. Funding for the Sloan Digital Sky Survey V has been provided by the Alfred P. Sloan Foundation, the Heising-Simons Foundation, the National Science Foundation, and the Participating Institutions. SDSS acknowledges support and resources from the Center for High-Performance Computing at the University of Utah. The SDSS web site is www.sdss.org.

References

- Aird, J., Coil, A. L., Georgakakis, A., et al. 2015, *MNRAS*, 451, 1892
- Antonucci, R. 1993, *ARA&A*, 31, 473
- Banados, E., Mazzucchelli, C., Momjian, E., et al. 2021, *ApJ*, 909, 80
- Banados, E., Schindler, J.-T., Venemans, B. P., et al. 2022, *ApJS*, 265, 29
- Bañados, E., Venemans, B. P., Decarli, R., et al. 2016, *ApJS*, 227, 11
- Bañados, E., Venemans, B. P., Morganson, E., et al. 2015, *ApJ*, 804, 118
- Becker, R. H., White, R. L., & Helfand, D. J. 1995, *ApJ*, 450, 559
- Belladitta, S., Moretti, A., Caccianiga, A., et al. 2023, *A&A*, 669, 134
- Braun, R., Bonaldi, A., Bourke, T., Keane, E., & Wagg, J. 2019
[arXiv:1912.12699]
- Caccianiga, A., Moretti, A., Belladitta, S., et al. 2019, *MNRAS*, 484, 204
- Cao, H. M., Frey, S., Gabányi, K. É., et al. 2017, *MNRAS*, 467, 950
- Chambers, K. C., Magnier, E. A., Metcalfe, N., et al. 2016, arXiv:1612.05560
[arXiv:1612.05560]
- Coppejans, R., Frey, S., Cseh, D., et al. 2016, *MNRAS*, 463, 3260
- Diana, A., Caccianiga, A., Ighina, L., et al. 2022, *MNRAS*, 5447, 5436
- Drlica-Wagner, A., Carlin, J. L., Nidever, D. L., et al. 2021, *ApJS*, 256, 2
- Drlica-Wagner, A., Ferguson, P. S., Adamów, M., et al. 2022, *ApJS*, 261, 38
- Drouart, G., Seymour, N., Galvin, T. J., et al. 2020, *PASA*, 37, 26
- Endsley, R., Stark, D. P., Fan, X., et al. 2022, *MNRAS*, 4261, 4248
- Evans, I. N., Primini, F. A., Glotfelty, K. J., et al. 2010, *ApJS*, 189, 37
- Evans, P. A., Page, K. L., Osborne, J. P., et al. 2020, *ApJS*, 247, 54
- Fan, X., Banados, E., & Simcoe, R. A. 2022, *ARA&A*, 61, 373
- Frey, S., Gurvits, L. I., Paragi, Z., & Gabányi, K. É. 2008, *A&A*, 484, L39
- Frey, S., Paragi, Z., Gurvits, L. I., Cseh, D., & Gabányi, K. É. 2010, *A&A*, 524, 7
- Frey, S., Paragi, Z., Gurvits, L. I., Gabányi, K. É., & Cseh, D. 2011, *A&A*, 531, L5
- Frey, S., Titov, O., Melnikov, A. E., de Vicente, P., & Shu, F. 2018, *A&A*, 618, 68
- Gabanyi, K. E., Cseh, D., Frey, S., et al. 2015, *MNRAS*, 450, 57
- Ghisellini, G., Della Ceca, R., Volonteri, M., et al. 2010, *MNRAS*, 405, 387
- Ghisellini, G., Perri, M., Costamante, L., et al. 2019, *A&A*, 627, 72
- Ghisellini, G. & Sbarrato, T. 2016, *MNRAS*, 461, L21
- Ghisellini, G., Sbarrato, T., Tagliaferri, G., et al. 2014, *MNRAS*, 440, 111
- Ghisellini, G. & Tavecchio, F. 2009, *MNRAS*, 397, 985
- Gilli, R., Norman, C., Calura, F., et al. 2022, *A&A*, 666, 17
- Gloude-mans, A. J., Duncan, K. J., Saxena, A., et al. 2022, *A&A*, 668, 27
- Gregory, P. C., Scott, W. K., Douglas, K., & Condon, J. J. 1996, *ApJS*, 103, 427
- Heckman, T. M. & Best, P. N. 2014, *ARA&A*, 52, 75
- Hurley-Walker, N., Galvin, T. J., Duchesne, S. W., et al. 2022, *PASA*, 39, e035
- Ighina, L., Caccianiga, A., Moretti, A., et al. 2019, *MNRAS*, 489, 2732
- Ighina, L., Caccianiga, A., Moretti, A., et al. 2021, *MNRAS*, 505, 4120
- Intema, H. T., Jagannathan, P., Mooley, K. P., & Frail, D. A. 2017, *A&A*, 598, 78
- Kellermann, K. I., Sramek, R., Schmidt, M., Shaffer, D. B., & Green, R. 1989, *AJ*, 98, 1195
- Koptelova, E. & Hwang, C.-Y. 2022, *ApJ*, 929, L7
- Kreuziger, M., Perger, K., Gabányi, K. É., et al. 2022, *ApJS*, 260, 49
- Lister, M. L., Homan, D. C., Hovatta, T., et al. 2019, *ApJ*, 874, 43
- Liu, Y., Wang, R., Momjian, E., et al. 2020, *ApJ*, 256, 2
- Liu, Y., Wang, R., Momjian, E., et al. 2022, *ApJ*, 939, 5
- Mainzer, A., Bauer, J., Cutri, R. M., et al. 2014, *ApJ*, 792, 30
- Merloni, A. 2016, *Astrophysical Black Holes, Lecture Notes in Physics*, Springer International Publishing Switzerland, 905, 101
- Merloni, A., Bongiorno, A., Brusa, M., et al. 2014, *MNRAS*, 437, 3550
- Merloni, A., Predehl, P., Becker, W., et al. 2012, eprint arXiv:1209.3114, 84
- Momjian, E., Bañados, E., Carilli, C. L., Walter, F., & Mazzucchelli, C. 2021, *AJ*, 161, 207
- Morabito, L. K., Sweijen, F., Radcliffe, J. F., et al. 2022, *MNRAS*, 515, 5758
- Moretti, A., Vattakunnel, S., Tozzi, P., et al. 2012, *A&A*, 548, 87
- Netzer, H. 2015, *ARA&A*, 53, 653
- Norris, R. P., Hopkins, A. M., Afonso, J., et al. 2011, *PASA*, 28, 215
- Norris, R. P., Marvil, J., Collier, J. D., et al. 2021, *PASA*, 38, 46
- Pacucci, F. & Loeb, A. 2021, *MNRAS*, 509, 1885
- Paliya, V. S., Ajello, M., Cao, H. M., et al. 2020, *ApJ*, 897, 177
- Radcliffe, J. F., Barthel, P. D., Thomson, A. P., et al. 2021, *A&A*, 649, 27
- Sbarrato, T., Ghisellini, G., Giovannini, G., & Giroletti, M. 2021, *A&A*, 655, A95
- Sbarrato, T., Ghisellini, G., Nardini, M., et al. 2012, *MNRAS*, 426, L91
- Sbarrato, T., Ghisellini, G., Nardini, M., et al. 2013a, *MNRAS*, 433, 2182
- Sbarrato, T., Ghisellini, G., Tagliaferri, G., et al. 2015, *MNRAS*, 446, 2483
- Sbarrato, T., Ghisellini, G., Tagliaferri, G., et al. 2022, *A&A*, 663, 147
- Sbarrato, T., Tagliaferri, G., Ghisellini, G., et al. 2013b, *ApJ*, 777, 147
- Schindler, J.-T., Fan, X., McGreer, I. D., et al. 2017, *ApJ*, 851, 13
- Shimwell, T. W., Hardcastle, M. J., Tasse, C., et al. 2022, *A&A*, 659, 1
- Spingola, C., Dallacasa, D., Belladitta, S., et al. 2020, *A&A*, 643, L12
- Stern, D., Djorgovski, S. G., Perley, R. A., de Carvalho, R. R., & Wall, J. V. 2000, *AJ*, 119, 1526
- Tadhunter, C. 2016, *A&ARv*, 24, 10
- Urry, C. M. & Padovani, P. 1995, *PASP*, 107, 803
- Vanden Berk, D. E., Richards, G. T., Bauer, A., et al. 2001, *AJ*, 122, 549
- Vijarnwanna-luk, B., Akiyama, M., Schramm, M., et al. 2022, *ApJ*, 941, 97
- Vito, F., Brandt, W. N., Yang, G., et al. 2018, *MNRAS*, 473, 2378
- Wayth, R. B., Tingay, S. J., Trott, C. M., et al. 2018, *PASA*, 35, 33
- Wu, J., Brandt, W. N., Miller, B. P., et al. 2013, *ApJ*, 763, 109
- Yang, G., Caputi, K. I., Papovich, C., et al. 2023, *ApJ*, 950, L5
- Zeimann, G. R., White, R. L., Becker, R. H., et al. 2011, *ApJ*, 736, 57
- Zhang, Y., An, T., Yang, X., et al. 2021, *MNRAS*, 507, 3736

Appendix A: Blazars and non-blazars in a flux limited sample

We tested the method presented by Ghisellini et al. (2019) and discussed in Sect. 2 (equation 1) using numerical simulations. Equation 1 gives the total number of jetted QSO expected in a flux-limited sample given the flux densities of all the blazars discovered in the same sample. To test this formula, we started from a population of un-beamed sources with an intrinsic (i.e. rest-frame) flux density ranging from 0.01 mJy to 100 mJy¹⁰ and randomly associated to each source a viewing angle. We then applied the beaming factor to these sources assuming different values of Γ (5, 10 and 15) and p (2 and 3) and considered only the sources above a certain flux limit (we use here 30 mJy that is the limit of the CLASS sample, but the results can be re-scaled to whichever value). We have then classified as blazars all the sources with $\theta < 1/\Gamma$ and applied equation 1 to recover the expected number of sources, both blazars and misaligned objects, above the flux limit. This value is then compared to the actual number of objects above the same limit.

We note that in these simulations we have assumed that there is no extended, un-beamed emission and, therefore, we expect that the value of N_{tot} provided by equation 1 should match exactly the actual value of sources given as input. In real data, extended emission may give a contribution although, as discussed in Sect. 2, we do not expect that this is relevant in the samples studied in this work.

Depending on the assumed values of the intrinsic flux density, Γ and p we obtain different values of total-to-blazar number ratio. Fig. A.1 shows the results of the comparison between the predicted ratio derived from equation 1 and the real one. It appears that equation 1 systematically overestimates (by a factor ~ 1.4) the true total number of sources in the sample (blue lines). The overestimate is nearly independent of the assumed value of the input parameters.

The origin of this discrepancy is likely related to the fact that equation 1 was derived assuming that all the blazars in the sample are oriented exactly at an angle equal to $1/\Gamma$. At this angle, the Doppler factor¹¹ is equal to Γ . This is clearly an approximation, since the actual viewing angles of a sample of blazars are expected to be distributed between 0° and $1/\Gamma$. A more correct number should be given by the average value of Doppler factor computed on all the sources observed within $1/\Gamma$. This average value is expected to be larger than Γ . The average Doppler factor for a sample of blazars is given by:

$$\frac{\int_0^{1/\Gamma} \delta(\theta) \sin(\theta) d\theta}{1 - \cos(1/\Gamma)} \sim 1.385\Gamma \quad (\text{A.1})$$

Including this correction in the derivation of equation 1 presented in Ghisellini & Sbarrato (2016), we obtain:

$$N_{tot} \sim \sum_{i=1}^N \left[1.44 \left(\frac{S_i}{S_{lim}} \right)^{1/p} - 1 \right] \quad (\text{A.2})$$

Again, we tested this relation through our numerical simulations (red line in Fig A.1) and we found that it correctly recovers the true total number of sources.

¹⁰ we have used different flux distributions, i.e. we started with luminosity functions with different slopes, but we found that the result does not depend on the assumed function.

¹¹ The Doppler factor is defined as $\delta = [\Gamma(1 - \beta \cos\theta)]^{-1}$, where Γ and β are the Lorentz factor and the ratio between the bulk velocity and the light speed respectively

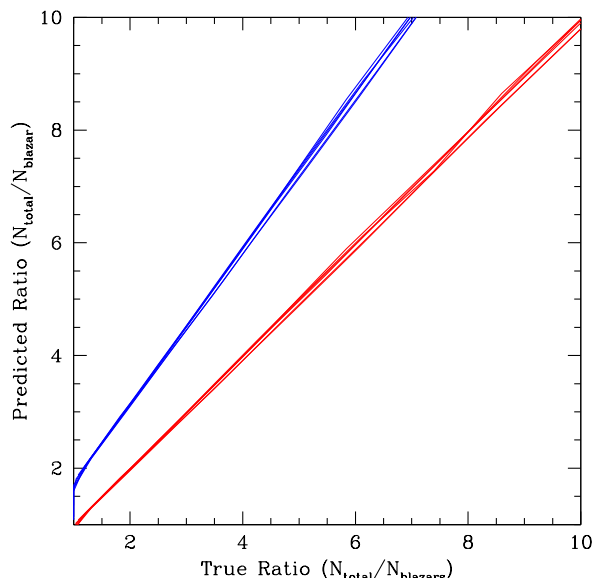


Fig. A.1: Results of a simulation where N jets of equal radio flux density have been randomly oriented in the sky and relativistically beamed according to the angle (θ) between the jet and the observer. We assume different values of the beaming parameters, i.e. $\Gamma=5, 10, 15$ and $p=2$ and 3 and different starting values of the un-beamed radio flux density (from 0.01 to 100 mJy). We then imposed a flux limit of 30 mJy and classified all the sources with $\theta < 1/\Gamma$ as blazars. These combinations of values yield different values (from 1 to 10) of the ratio between total number of sources (blazar+misaligned objects) and blazars that are included in the simulated blazar sample. We finally applied Eq 1 and Eq 2 to the simulated blazar sample (assuming the correct value of p) to recover the expected total number of sources above the flux limit. In the figure, we compare the predicted total/blazar number ratio with the true one. Equation 1 (blue line) systematically overestimates the result by a factor ~ 1.4 while equation 2 (red line) provides the correct results

Appendix B: Reliability of the classifications

As mentioned in Sect. 4.1, the classification of a source as blazar is not straightforward, and it may depend on the adopted method. Recently, Krezinger et al. (2022) pointed out some discrepancies between the classification based on the SED analysis and the one based on VLBI data. Among the high- z QSO in the samples considered here, there are 16 objects with a classification from the literature based on VLBI data. While in most (70%) cases the two classifications agree, in 5 cases there seems to be a disagreement. These cases are discussed below.

J083946.2+511202 - This source is classified as blazar based on the $\tilde{\alpha}_{ox}$ ($=1.25$). The blazar nature is also suggested by the analysis of the SED (Sbarrato et al. 2013a). Quite consistently to this classification, VLBI data (Cao et al. 2017) show a flat-spectrum, variable and quite compact core. However, the T_b estimated from the deconvolved size ($3.0 \pm 0.5 \times 10^{10}$ K) is close but below the equipartition limit. This is likely a borderline source (also from the $\tilde{\alpha}_{ox}$ point of view) whose exact orientation could be near the one expected for blazars.

J103717.7+182303 - The value of $\tilde{\alpha}_{ox}$ of this object is similar to the one computed for the previous source (1.28) and is suggestive of a blazar nature. From the analysis of the SED Sbarrato et al. (2022) conclude that this source is either a

blazar or a source viewed at the border of the definition. Again, VLBI data seem to resolve the emission finding a relatively low value of T_b ($2.6 \pm 0.5 \times 10^9$ K), below the equipartition limit (Kreuzinger et al. 2022). As for J083946.2+511202, this could be a source at the border of the blazar definition.

J114657.8+403708 - Also this object is classified as blazar on the basis of the X-ray data ($\tilde{\alpha}_{ox}=1.31$) and of the SED (Ghisellini et al. 2014) but the value of T_b derived from VLBI data ($4.5 \pm 0.3 \times 10^9$ K) is below the equipartition limit (Frey et al. 2010).

J123142.1+381659 - The value of $\tilde{\alpha}_{ox}$ computed for this object (1.18) indicates a blazar nature. The same classification is reported in Sbarrato et al. (2022) while Kreuzinger et al. (2022) suggest that the source is misaligned on the basis of the relatively low T_b ($1.36 \pm 0.27 \times 10^9$ K).

J142048.0+120546 - Again, we classified this source as blazar due to its low $\tilde{\alpha}_{ox}$ (1.21) and this classification is supported by the analysis of the SED (Sbarrato et al. 2015). VLBI observations with EVN, instead, reveal a double morphology on a scale of $1.33''$, which is too compact to be detected by FIRST data (Cao et al. 2017). The most compact and brightest component, that is positionally coincident with the optical position of the QSO, has a relatively high T_b ($4.0 \pm 1.0 \times 10^9$ K) but below the equipartition limit.

To summarize, all the 5 cases of inconsistent classification between the two methods are quite similar and include sources with values of $\tilde{\alpha}_{ox}$ below but close to the limit of 1.355 (typically 1.2-1.3) and show brightness temperature relatively high (above 10^9 K) but below the equipartition limit ($0.3\text{-}5 \times 10^{10}$ K). At the same time, we have other 4 sources with similar values of $\tilde{\alpha}_{ox}$ ($\sim 1.2\text{-}1.3$) but for which VLBI observations confirm the presence of boosting.

All the remaining 7 objects with VLBI data, i.e. sources with either a very low value of $\tilde{\alpha}_{ox}$ (between 0.8 and 1.1, 4 objects) or a value above 1.355 (classified as non-blazars, 3 objects) have a consistent classification from VLBI data.

We conclude that the two methods are in reasonably good agreement, except for sources that are borderline ($\tilde{\alpha}_{ox}$ between 1.2 and 1.3). In this range, $\sim 50\%$ of the sources have a VLBI classification that seems to contradict the one inferred from the X-ray data. As already said, these are cases that require a more careful analysis that takes into account all the possible pieces of information available. We stress here that also the VLBI classification can be uncertain when the measured extensions, critical to determine the value of T_b , are only fractions of the synthesized beam and when the flux densities are relatively low compared to the local RMS. Only a synergic use of all the available multi-wavelength data can provide the best possible classification.

In any case, as discussed in Sect. 4.2, if we do not consider as blazars the sources with controversial classification, the results presented in this paper do not change significantly.

Appendix C: The samples

In Tab C.1 we present the complete list of sources used in this paper. For each source in the CLASS and FIRST samples, we give the following quantities. Column 1: name based on the optical coordinates. Column 2-3: optical position. Columns 4: redshift derived from Caccianiga et al. (2019) or from SDSS except for four objects: ¹Bañados et al. (2015), ²Gloude-mans et al. (2022), ³Bañados et al. (2021), ⁴Stern et al. (2000). Column 5: mag_{drop} corrected for Galactic reddening. The filter is specified between parenthesis. Magnitudes are taken from Pan-STARRS1 survey (PS1, Chambers et al. 2016) or from the DECam Local Volume

Exploration Survey (DELVE, Drlica-Wagner et al. 2021, 2022); Column 6: 1.4 GHz peak flux density from FIRST. Column 7: 5 GHz flux density from GB6 catalogue (Gregory et al. 1996). Column 8: non-simultaneous radio spectral index ($S_\nu \propto \nu^{-\alpha}$) from 1.4 GHz and 144/150 MHz using FIRST and LoTSS (Shimwell et al. 2022) or TGSS (Intema et al. 2017) integrated flux densities. Column 9: sample: F=FIRST sample, C=CLASS sample. Column 10: Log of radio-loudness computed using 1.4 GHz flux density, and assuming the radio slope given in column 8 or assuming $\alpha_r=0.1$, and using the near-infrared magnitude at 3.4 micron (W1) from Wide-field Infrared Survey Explorer (NEOWISE, Mainzer et al. 2014) which provides the photometric point closest to 4400\AA rest-frame wavelength for $z \geq 4$ sources. To obtain the monochromatic flux at 4400\AA we use the spectral index computed between W1 and z-filter (or y-filter for $z > 6.3$ sources). If W1 is not available, we compute R using the z magnitude and assuming $\alpha_0=0.44$ (Vanden Berk et al. 2001); Column 11: The two-points-spectral index from radio to X-rays ($\tilde{\alpha}_{ox}$). This is either taken from Ighina et al. (2019), for the sources in the CLASS sample, or computed using the available X-ray fluxes and the magnitudes in z-filter. As for the radio-loudness parameter, we use the optical spectral index computed between W1 and z-filter, if available, or assume $\alpha_0=0.44$. The error on this parameter is mostly due to the uncertainty on the optical/UV slope and on the X-ray fluxes. Considering the range of values of slopes reported in Table 5 of Vanden Berk et al. (2001) (0.33-0.93) and the typical errors on the X-ray fluxes, we derive a typical error on $\tilde{\alpha}_{ox}$ of $-0.03, +0.06$. Column 12: classification based on X-ray data: b=blazar ($\tilde{\alpha}_{ox} \leq 1.355$), nb=non-blazar ($\tilde{\alpha}_{ox} > 1.355$).

Table C.1: The sample of high-z jetted QSO

name	RA (J2000) (2)	DEC (J2000) (3)	z (4)	mag _{drop} (5)	S_{FIRST}^{pk} [mJy] (6)	S_{GB6} [mJy] (7)	α_R (8)	sample (9)	logR (10)	$\bar{\alpha}_{ox}$ (11)	class
J001115.2+144601	2.81348	14.76718	4.97	18.20±0.01 (i)	24.0	31	0.14	C	2.1	1.17	b
J003126.8+150739	7.86167	15.12764	4.28	20.00±0.01 (r)	43.0	93	-	C	2.8	1.40	nb
J012126.1+034706	20.35898	3.78515	4.13	18.68±0.01 (r)	73.0	51	-	C	2.4	1.41	nb
J012201.9+031002	20.50792	3.16733	4.00	20.85±0.02 (r)	106.1	96	-0.07	C	3.6	0.79	b
J083549.4+182520	128.95594	18.42225	4.41	20.79±0.02 (r)	51.5	40	0.21	C	3.2	1.03	b
J083946.2+511202	129.94259	51.20080	4.40	19.35±0.01 (r)	40.5	51	-0.13	C	2.2	1.25	b
J090132.6+161506	135.38604	16.25190	5.63 ¹	20.69±0.03 (z)	3.0	<30	-	F	1.9	1.33	b
J090630.7+693030	136.62813	69.50856	5.47	19.77±0.03 (z)	-	106	-	C	3.2	1.05	b
J091316.5+591921	138.31899	59.32267	5.12	20.58±0.02 (i)	17.4	<30	-0.33	F	3.2	1.60	nb
J091824.3+063653	139.60158	6.61481	4.19	19.60±0.01 (r)	25.9	36	-	CF	2.1	1.26	b
J092132.7+185654	140.38648	18.94860	4.52	21.00±0.04 (i)	4.3	<30	-	F	2.0	-	-
J092709.6+282229	141.79038	28.37476	4.30	20.19±0.01 (r)	1.9	<30	-0.09	F	1.7	-	-
J094004.8+052630	145.02000	5.44194	4.50	20.75±0.02 (i)	55.7	<30	0.87	F	3.4	1.09	b
J094409.5+100656	146.03968	10.11575	4.76	19.17±0.01 (i)	0.6	<30	-	F	0.7	-	-
J100303.4+112209	150.76435	11.36938	4.58	20.83±0.02 (i)	2.3	<30	-	F	2.2	-	-
J100645.5+462717	151.68999	46.45479	4.44	20.61±0.02 (r)	6.0	<30	-0.39	F	2.2	-	-
J100903.3+174950	152.26404	17.83067	4.05	20.77±0.02 (r)	0.5	<30	-	F	1.5	-	-
J101337.8+351849	153.40779	35.31384	5.03 ²	20.58±0.02 (i)	1.6	<30	0.20	F	1.5	-	-
J101506.6+281757	153.77790	28.29942	4.15	19.85±0.01 (r)	1.1	<30	0.12	F	1.3	-	-
J102043.8+000105	155.18258	0.01830	4.19	20.40±0.01 (r)	1.7	<30	-	F	1.4	-	-
J102249.2+130125	155.70530	13.02363	4.03	19.36±0.01 (r)	2.6	<30	-	F	0.7	-	-
J102343.1+553132	155.92974	55.52566	4.46	20.59±0.02 (r)	2.0	<30	-0.17	F	1.0	-	-
J102623.6+254259	156.59845	25.71651	5.25	19.92±0.01 (i)	230.8	142	0.25	CF	3.6	1.15	b
J103418.6+203300	158.57771	20.55006	5.01	19.75±0.01 (i)	4.0	<30	-	F	1.5	-	-
J103446.5+110214	158.69393	11.03736	4.27	18.82±0.01 (r)	0.9	<30	-	F	0.8	-	-
J103601.0+500831	159.00429	50.14215	4.48	20.08±0.01 (r)	9.2	<30	0.35	F	1.7	-	-
J103717.7+182303	159.32386	18.38418	4.04	19.89±0.01 (r)	13.6	<30	-	F	2.3	1.28	b
J104007.3+161809	160.03066	16.30265	4.08	20.96±0.02 (r)	3.7	<30	-	F	1.4	-	-
J104742.5+094744	161.92741	9.79581	4.25	20.51±0.01 (r)	18.9	<30	0.17	F	2.4	-	-
J105756.2+455553	164.48446	45.93140	4.13	17.63±0.01 (r)	1.1	<30	1.14	F	0.2	1.56	nb
J110201.9+533912	165.50797	53.65351	4.31	20.35±0.01 (r)	4.5	<30	0.47	F	2.1	-	-
J110549.9+290225	166.45798	29.04030	4.07	20.49±0.02 (r)	3.9	<30	0.40	F	2.2	-	-
J111639.7+092612	169.16552	9.43668	4.13	20.33±0.01 (r)	1.4	<30	-	F	1.6	-	-
J112925.3+184624	172.35560	18.77340	6.82 ³	20.74±0.09 (y)	1.0	<30	-	F	1.8	-	-
J113729.4+375224	174.37262	37.87340	4.24	19.95±0.01 (r)	2.7	<30	-0.09	F	1.8	-	-
J114657.8+403708	176.74084	40.61911	5.01	19.40±0.01 (i)	12.4	<30	-0.67	F	1.9	1.31	b
J121134.3+322615	182.89330	32.43757	4.14	19.56±0.01 (r)	3.7	<30	0.44	F	1.2	-	-
J121329.0+181029	183.37114	18.17476	4.50	20.08±0.01 (i)	2.3	<30	-	F	2.1	-	-
J123142.1+381659	187.92554	38.28311	4.14	20.11±0.02 (r)	20.4	<30	0.36	F	2.7	1.18	b
J123237.4+520343	188.15623	52.06218	4.61	20.55±0.03 (i)	3.6	<30	-0.42	F	2.2	-	-
J123239.2+525250	188.16373	52.88083	4.34	18.44±0.01 (r)	0.5	<30	-	F	0.3	-	-
J123604.1+030341	189.01747	3.06163	4.58	19.98±0.01 (i)	2.0	<30	-	F	1.5	-	-
J124230.5+542257	190.62744	54.38261	4.73	19.82±0.01 (i)	19.7	<30	0.16	F	2.4	1.41	nb
J124943.6+152707	192.43196	15.45196	4.02	19.34±0.01 (r)	1.8	<30	-	F	1.2	-	-
J130002.1+011823	195.00902	1.30641	4.61	18.88±0.01 (i)	2.7	<30	-	F	1.1	1.27	b
J130738.8+150752	196.91180	15.13114	4.08	19.98±0.01 (r)	3.4	<30	-	F	1.8	-	-
J130940.7+573309	197.41960	57.55277	4.28	19.57±0.01 (r)	10.7	<30	-0.15	F	1.6	1.35	b
J131121.3+222738	197.83886	22.46075	4.61	20.45±0.02 (i)	6.5	<30	-	F	2.1	1.37	nb
J131814.0+341805	199.55846	34.30156	4.88	19.13±0.01 (i)	3.7	<30	-0.49	F	1.0	-	-
J132512.4+112329	201.30206	11.39160	4.41	19.45±0.01 (r)	69.4	62	-	CF	2.6	1.31	b
J133422.6+475033	203.59431	47.84267	4.95	19.59±0.01 (i)	0.6	<30	0.98	F	1.1	1.48	nb
J134811.2+193523	207.04690	19.58990	4.40	20.66±0.02 (r)	49.3	38	0.00	CF	3.0	1.23	b
J135135.7+284014	207.89879	28.67078	4.72	19.66±0.01 (i)	3.2	<30	-0.47	F	1.7	-	-
J135554.5+450421	208.97733	45.07252	4.10	19.55±0.01 (r)	1.5	<30	-0.58	F	1.5	-	-
J140025.4+314910	210.10587	31.81961	4.64	20.20±0.01 (i)	20.2	<30	-0.06	F	2.7	1.23	b
J140034.0+173031	210.14186	17.50872	4.29	20.74±0.02 (r)	1.6	<30	-	F	1.4	-	-
J140850.9+020522	212.21215	2.08964	4.01	18.98±0.01 (r)	1.5	<30	-	F	1.2	1.40	nb
J141209.9+062406	213.04155	6.40191	4.36	20.00±0.01 (r)	43.0	34	0.43	CF	3.1	1.29	b
J142048.0+120546	215.20004	12.09611	4.03	19.80±0.01 (r)	83.8	47	0.66	CF	3.2	1.21	b
J142308.2+224158	215.78435	22.69946	4.32	19.83±0.01 (r)	35.1	22	-	F	2.7	1.33	b
J142634.8+543622	216.64524	54.60634	4.85	19.90±0.01 (i)	4.3	<30	-0.18	F	1.8	-	-
J143023.7+420436	217.59891	42.07681	4.71	19.78±0.01 (i)	211.3	337	-0.10	CF	3.4	0.82	b
J143413.0+162852	218.55441	16.48131	4.21	19.83±0.01 (r)	4.8	<30	-	F	1.7	-	-
J143942.9+012741	219.92911	1.46161	4.16	20.43±0.02 (r)	3.7	<30	-	F	1.7	-	-
J144231.7+011055	220.63216	1.18203	4.49	20.14±0.01 (i)	1.1	<30	-	F	1.9	1.27	b
J144720.5+164018	221.83575	16.67167	4.07	20.43±0.02 (r)	1.1	<30	-	F	1.4	-	-
J145224.2+335424	223.10106	33.90684	4.12 ⁴	20.40±0.01 (r)	6.8	<30	-0.22	F	1.8	-	-
J145628.9+200727	224.12072	20.12419	4.26	19.51±0.01 (r)	0.7	<30	-	F	0.6	-	-
J145924.0+035622	224.85030	3.93951	4.13	20.54±0.01 (r)	3.3	<30	-	F	1.6	-	-

Table C.1: continued

J150149.0+592252	225.45436	59.38119	4.65	18.84±0.01 (i)	4.6	<30	0.71	F	1.5	-	-
J150544.6+433824	226.43583	43.64019	4.68	18.82±0.01 (i)	5.0	<30	0.11	F	1.2	-	-
J150912.2+202653	227.30100	20.44832	4.06	20.85±0.02 (r)	6.3	<30	-	F	2.4	-	-
J151002.9+570243	227.51219	57.04539	4.31	20.48±0.03 (r)	248.1	292	0.11	CF	3.5	0.94	b
J152028.1+183556	230.11726	18.59894	4.12	19.60±0.01 (r)	6.3	<30	-	F	2.3	>1.50	nb
J152028.1+210039	230.11734	21.01101	4.55	20.12±0.02 (i)	1.1	<30	-	F	1.9	-	-
J152404.2+134417	231.01763	13.73821	4.79	19.32±0.01 (i)	0.5	<30	-	F	0.7	-	-
J152759.0+344118	231.99600	34.68840	4.32	20.92±0.03 (r)	4.7	<30	0.30	F	2.4	-	-
J153533.8+025423	233.89120	2.90650	4.39	20.43±0.01 (r)	78.8	53	0.40	CF	3.6	0.93	b
J153830.7+424405	234.62799	42.73489	4.10	20.85±0.03 (r)	11.7	<30	-0.22	F	2.6	>1.35	nb
J154824.0+333500	237.10006	33.58336	4.68	20.77±0.02 (i)	37.6	<30	0.54	F	3.6	0.96	b
J161216.7+470253	243.06981	47.04823	4.35	20.62±0.02 (r)	52.3	30	0.18	C	2.9	1.39	nb
J162957.2+100023	247.48867	10.00653	5.00	20.45±0.02 (i)	51.5	33	0.50	C	3.5	1.09	b
J164854.5+460327	252.22721	46.05761	5.36	20.29±0.01 (i)	32.0	30	0.21	C	2.8	1.34	b
J171105.5+383004	257.77308	38.50121	4.00	20.41±0.02 (r)	49.1	36	-0.22	C	3.0	1.15	b
J222032.5+002537	335.13542	0.42708	4.20	20.04±0.01 (r)	61.9	37	0.91	C	3.3	1.26	b
J231448.7+020151	348.70296	2.03086	4.11	19.67±0.01 (r)	117.8	84	-0.05	C	3.1	1.25	b
J235758.5+140201	359.49396	14.03384	4.33	20.25±0.01 (r)	-	78	0.18	C	3.3	1.02	b